Research Article | Vol. 28, No. 2 / 20 January 2020 / Optics Express 1827

Optics EXPRESS

Photonic independent component analysis using an on-chip microring weight bank

PHILIP Y. MA,[1,*] ALEXANDER N. TAIT,[1,2] THOMAS FERREIRA DE LIMA,[1] CHAORAN HUANG,[1] BHAVIN J. SHASTRI,[1,3] AND PAUL R. PRUCNAL[1]

[1]*Department of Electrical Engineering, Princeton University, Princeton, NJ 08544, USA*
[2]*Physical Measurement Laboratory, National Institute of Standards and Technology, Boulder, CO 80305, USA*
[3]*Department of Physics, Engineering Physics and Astronomy, Queen's University, Kingston, ON K7L 3N6, Canada*
[*]*yechim@princeton.edu*

Abstract: Independent component analysis (ICA) is a general-purpose technique for analyzing multi-dimensional data to reveal the underlying hidden factors that are maximally independent from each other. We report the first photonic ICA on mixtures of unknown signals by employing an on-chip microring (MRR) weight bank. The MRR weight bank performs so-called weighted addition (i.e., multiply-accumulate) operations on the received mixtures, and outputs a single reduced-dimensional representation of the signal of interest. We propose a novel ICA algorithm to recover independent components solely based on the statistical information of the weighted addition output, while remaining blind to not only the original sources but also the waveform information of the mixtures. We investigate both channel separability and near-far problems, and our two-channel photonic ICA experiment demonstrates our scheme holds comparable performance with the conventional software-based ICA method. Our numerical simulation validates the fidelity of the proposed approach, and studies noise effects to identify the operating regime of our method. The proposed technique could open new domains for future research in blind source separation, microwave photonics, and on-chip information processing.

© 2020 Optical Society of America under the terms of the OSA Open Access Publishing Agreement

1. Introduction

Independent component analysis (ICA) is among the oldest representation learning algorithms that transform the data in such a way that its latent structure can be made more visible and accessible [1], [2]. As a classical unsupervised learning method, ICA has been widely explored in terms of performing feature extraction [3], face recognition [4], and action recognition [5] on digital images and videos. ICA has particularly served as the primary time-series analysis solution to blind source separation (BSS) problems, aiming to reveal independent latent variables from the observed multivariate (two or more) mixtures without a priori knowledge on the mixing process [6]. Examples include successful source recovery [7] and noise removal [8] from physiological measurements, and effective separation on speech [9] and audio signals [10].

Meanwhile, microwave communications has witnessed ever-increasing spatio-spectral utilizations owing to the incipient proliferation of multi-antenna approaches (e.g., multiple-input multiple-output (MIMO) technology) and opportunistic methods (e.g., cognitive radio) [11]. The expansion of wireless transmissions demands new regulatory means where ICA could be the key enforcer of necessary interference cancellation [12] and spectrum monitoring [13]. Contemporary ICA techniques in radio-frequency (RF) systems rely heavily on front-end analog-to-digital converters (ADCs) to sample and quantize inputs for back-end digital signal processing (DSP), both of which are facing fundamental trade-offs among channel dimensionality, processing bandwidth, and power consumption [14–16]. Moreover, analog electronic approaches rely on

#383603 https://doi.org/10.1364/OE.383603
Journal © 2020 Received 19 Nov 2019; revised 27 Dec 2019; accepted 27 Dec 2019; published 13 Jan 2020

Optics EXPRESS

frequency dependent microwave electronics that exhibit poor reconfigurability and tunability across wideband RF spectrum [17].

Lately, a photonic architecture was proposed for networking and computation on wavelength-division multiplexing (WDM) signals using standard photonic integrated circuit (PIC) components [18]. This architecture enables a parallel matrix-vector multiplication operation called weighted addition, where an array of microrings (MRRs) performs channel-wise weighting (i.e., spectral filtering) on individual WDM signals while a balanced photo-detector (BPD) outputs the sum of weighted signals on all channels [19]. The MRRs carry at least two advantages: a) they are compact passive devices with small footprint ($\sim$100 μm^2) but holding high operational bandwidth (>10 GHz), which enables unparalleled information density if instantiated into a dense weight bank; b) they have wide tunability (over THz bandwidth) achieved by thermal tuning [20], which equips them with the capability of performing frequency independent processing on arbitrary RF signals. Therefore, MRRs have been adopted as the key reconfigurable elements in directed-logic circuits [21], waveform generation [22], reservoir computing [23], and neuromorphic photonic architectures [24,25].

In this paper, we present the first demonstration of photonic ICA using an on-chip MRR weight bank to identify the underlying sources that form the basis of the observed data. Source separation is a critical extension to our prior work on photonic principal component analysis (PCA) that only decomposes the data to uncorrelated components [26]. We follow the methodology of multivariate photonics assuming the waveform information of received mixtures may not be readily available in realistic field scenarios [13,27], and demonstrate that such information is unnecessary for ICA task but requires sophisticated front-end ADCs and additional data storage. Instead, we propose a novel photonic ICA algorithm that is able to extract independent components (ICs) solely based on the higher-order statistics of a single reduced-dimensional weighted addition output. We deploy a prototype implementation consisting of an RF subsystem that can dynamically reconfigure the mixing process of two independent sources, and a photonic subsystem that accomplishes record-high accuracy and precision on MRR weight control. Our proof-of-concept experiment of two-channel photonic ICA achieves performance whose accuracy and repeatability are close to that of conventional software-based ICA method (i.e., FastICA [28]) under different channel separability and near-far conditions. In addition, our numerical simulation further studies how the Gaussian noise affects the performance of photonic ICA procedure, and identifies the operating regimes where our approach holds its fidelity. Overall, the proposed photonic ICA scheme paves the way for future research on integrated photonic systems that could enable advanced BSS pipelines for more complicated information mixing process.

2. Theory

In this section, we provide a succinct exposition of the basic ICA theory. Our photonic ICA scheme follows the same two-step procedure as most ICA algorithms: a preliminary whitening and the actual ICA estimation [29].

2.1. Definition

Consider we have source matrix $\mathbf{S}$ where each row represents an independent time-series signal $s_i(t)(i = 1, \ldots, n)$. These signals are mixed and result in the observed mixtures $\mathbf{X} = \mathbf{AS}$ with the mixing coefficients collectively placed in the mixing matrix $\mathbf{A}$. ICA aims to figure out the corresponding inverse matrix of $\mathbf{A}$, called the demixing matrix $\mathbf{A^{-1}}$, such that we can retrieve the independent sources by multiplying it with the received mixtures $\bar{\mathbf{S}} = \mathbf{A^{-1}X} = \mathbf{A^{-1}AS}$.

2.2. Whitening using PCA

Whitening applies a whitening matrix $\mathbf{V}$ to transforms the mixtures such that $\mathbf{Z} = \mathbf{VX} = \mathbf{VAS}$ is white: expectation $E(\mathbf{ZZ^T}) = \mathbf{I}$, where $\mathbf{I}$ is the identity matrix. Whitening has one of its

Optics EXPRESS

straightforward solutions from PCA: $\mathbf{V} = \mathbf{U}\Sigma^{-1/2}\mathbf{U}^{\mathbf{T}}$, where $\mathbf{U}$ has principal component (PC) vectors as its columns while diagonal matrix Σ has PC variances as its diagonal entries. Since ICA cannot determine the power (variance) of ICs (as scaling does not break independence), it is commonly assumed for the estimated ICs to hold $E(\bar{\mathbf{S}}\bar{\mathbf{S}}^{\mathbf{T}}) = \mathbf{I}$. In that case, whitening successfully reduces the ICA problem to finding an orthogonal transformation $\mathbf{Q}$ (i.e., a rotation) such that $\bar{\mathbf{S}} = \mathbf{QZ} = \mathbf{QVX} = \mathbf{QVAS}$. The search for $\mathbf{Q}$ is easier than direct search for $\mathbf{A}^{-1}$ because there are fewer degree of freedom.

2.3. ICA using non-Gaussianity

ICA searches for $\mathbf{Q}$ by drawing inspiration from the central limit theorem, which states that the sum of independent sources is more Gaussian than any of the individual sources. It leads to a straightforward conclusion that ICs are supposed to maximize their relative distance from the Gaussian distribution, i.e., the non-Gaussianity. We adopt kurtosis, a fourth-order moment, as the measurement of non-Gaussianity in this work. More specifically, given an IC estimation y, we use its relative kurtosis to Gaussian distribution

$$kurt(y) = \frac{\mu_4(y)}{\sigma^4(y)} - 3 \tag{1}$$

where μ_4 is the fourth-order central moment, σ is the standard deviation, and 3 is the kurtosis of the Gaussian distribution. Our method parallels that of maximization of differential entropy (i.e., neg-entropy) [30], but contrasts to other prior ICA studies that require the approximation of probability distribution function of sources, including methods based on minimization of mutual information between estimated components [2], and maximum-likelihood estimation [31].

3. Methods

The experimental setup of photonic ICA is shown in Fig. 1(a). Two distributed feedback lasers (DFBs) generate optical carriers at 1548.52 nm and 1550.12 nm, respectively. Each optical carrier is modulated at a Mach-Zehnder modulator (MZM) by the data pattern from an arbitrary wave generator (AWG, Agilent 33220A) and multiplexed together at a WDM multiplexer (MUX). The silicon photonic chip is mounted on a temperature-controlled fiber alignment stage. The WDM signals enter the MRR weight bank at the IN port, and leave at the THRU and DROP ports. All lights are guided onto/off the chip via TE focusing grating couplers. The insertion loss is about 5 dB per grating coupler, and there is an 1 dB waveguide/bending loss (so insertion loss is 10-12 dB round-trip). The outputs at THRU and DROP ports are summed off-chip by a balanced photo-detector (BPD, Discovery Semiconductors DSC-R405ER) to enable weights in the continous range of [-1, +1]. The resulted electrical output of BPD is recorded by a sampling oscilloscope (Oscope, Tektronix DSA8300). Each MRR is driven by a source meter (SM, Keithley 2400) set in current-source, voltage-measure mode. AWGs, Oscope, and SMs are all computer-controlled by *lightlab* software [32].

Our silicon photonic chip was fabricated at Advanced Micro Foundry (AMF) A*STAR foundry [34]. Silicon thickness is 220 nm, and buried oxide thickness is 2 μm. The waveguides of 500 nm width are patterned fully through to the oxide by deep ultraviolet lithography. The MRR weight bank, as shown in Fig. 1(b), consists of ring waveguides evanescently coupled to bus waveguides in a parallel add-drop configuration. The WDM signals enter the MRR weight bank at the IN port, and each wavelength is directed to the THRU and DROP ports in a controllable ratio depending on its resonance condition with the corresponding MRR. Each deposited metal trace (at the top) can be probed by an SM, delivering the tuning current to thermally control the resonance position of individual MRRs. The same ground trace (at the bottom) is shared among MRRs to reduce the electrical I/O count.

Optics EXPRESS

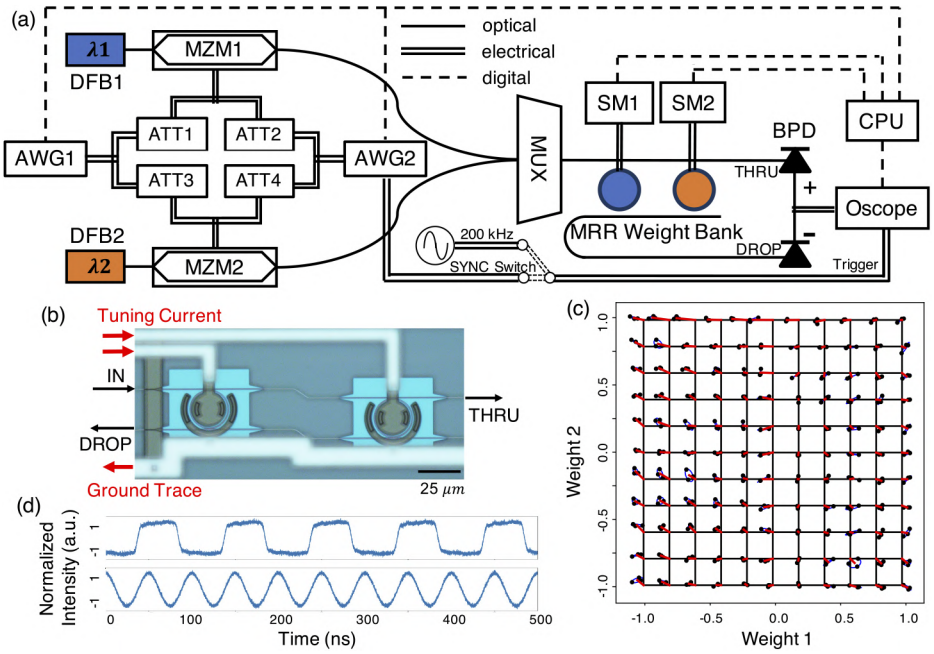

Fig. 1. (a) Schematic of the experimental setup for performing photonic ICA using an on-chip MRR weight bank. DFB: distributed feedback laser, MZM: Mach-Zehnder modulator, ATT: RF attenuator, AWG: arbitrary wave generator, MUX: WDM multiplexer, SM: source meter, BPD: balanced photo-detector, Oscope: sampling oscilloscope. The synchronization (SYNC) switch toggles the Oscope triggering state between a repeating pattern from AWG and a free-running clock at 200 kHz. (b) Micrograph of the fabricated MRR weight bank. MRRs are coupled with two bus waveguides that input the WDM signals at the IN port, and output the weighted WDM signals at the THRU and DROP ports. Metal traces are deposited to deliver the tuning current to the MRR weight bank to thermally tune the optical transmission of MRRs to configure their weights. (c) Two-channel weight evaluation results in the same format of [26,33]. Black grid crossings are the target weights. Red lines represent the deviation between the target weights and the mean of measured weights over 3 repetitions. Blue ellipses represent the standard deviation of measured weights over 3 repetitions. (d) Example of IC sources generated by two AWGs; top: square wave with kurtosis of 2, and bottom: sinusoidal wave with kurtosis of 1.5.

We list here some basic characterizations on the two MRRs used in this work, with more details described in [26] as we use the same chip for both photonic PCA and ICA. The two MRRs have radii of 10.921 μm and 10.937 μm, respectively. Their bare resonance peaks are at 1547.73 nm and 1549.24 nm. For both MRRs, the free spectral range (FSR) is 8.62 nm and finesse F is 30.79. The coupling gap between the bus waveguides and ring waveguide is 200 nm, and the Q factor is approximately 5500. To enable feedback control on the MRR weight bank through in-ring photoconductive heaters [33,35], an N-doped section of 10 μm width is patterned to follow MRRs, outside of which heavy N++ doping is used to make ohmic contacts. Phosphorous dopant concentrations are N: $5 \times 10^{17} cm^{-3}$ and N++: $5 \times 10^{20} cm^{-3}$ as in [36]. The thermal tuning efficiency of MRRs is measured to be 0.15 nm/mW. We perform MRR weight bank calibration using the feedback control procedure [33], and achieve 5.7 bits of accuracy (1.9% error, red lines) and 6.9 bits of precision (0.84% error, blue ellipses) as shown in Fig. 1(c). Such accomplishment improves upon the latest weight accuracy/precision record (5.2 bits of accuracy and 6.3 bits of precision) set by our recent photonic PCA work [26].

Optics EXPRESS

We employ two AWGs as the independent sources in our two-channel photonic ICA experiment. One AWG generates square wave (10 MHz) whose kurtosis is 2. The other AWG generates sinusoidal wave (20 MHz) whose kurtosis is 1.5. Examples of IC sources are shown in Fig. 1(d), which will be used as the ground-truth in later performance evaluation phase (with some temporal shift for alignment purpose). These two signals are mixed by a dedicated mixer consisting of four tunable RF attenuators (ATTs). As shown in Fig. 1(a), these four ATTs are inter-connected in such a way that a) ATT1 and ATT3 receive the source signal from AWG1, while ATT2 and ATT4 receive the source signal from AWG2; and that b) the outputs from ATT1 and ATT2 are combined as the input to MZM1, while the outputs from ATT3 and ATT4 are combined as the input to MZM2. As a result, we have an effective mixing matrix

$$\mathbf{A} = \begin{bmatrix} a_1 & a_2 \\ a_3 & a_4 \end{bmatrix} \tag{2}$$

where each mixing coefficient $a_i (i = 1, 2, 3, 4)$ represents the attenuation of corresponding ATT. In our prototype implementation, the attenuation of each ATT is in the range of 0–12 dB, so a_i is in the range of [0.25, 1].

We also use a synchronization (SYNC) switch to swap between two triggering conditions for the Oscope [26]. The motivation is that the input mixtures and weighted addition output are generally not synchronized with the Oscope in field (i.e., real life) scenarios. The only way to obtain an accurate digital waveform is to take samples in a real-time order at a real-time rate greater than the Nyquist frequency, which relies on sophisticated front-end ADCs and DSP systems. Instead, our photonic ICA approach treats the complete waveform information from input mixtures as redundancy, and only requires observing certain statistical properties of the weighted addition output produced by our simple photonic front-end (MRR weight bank plus BPD). We emulate such constrained observability by triggering the Oscope with a 200 kHz clock (i.e., the internal clock on Oscope) to operate it in the free-running mode such that the signal can only be sampled at a sub-Nyquist rate (200 kS/s here). Occasionally when the waveform information is needed, the Oscope can be synchronized with the AWGs to synthesize the accurate waveform at a super-Nyquist sampling rate (16 GS/s here). These cases (as will be seen in later sections) include acquiring the IC waveforms for performance evaluation, and implementing the software-based ICA algorithm to obtain the baseline results.

4. Photonic ICA

We propose a novel photonic ICA algorithm that overcomes the above constrained observability, and interacts with the photonic hardware to deliver ICs in a straightforward way. As shown in Fig. 2, the MRR weight bank and BPD pair receives the WDM signals carrying the input mixtures $\mathbf{X}$, and produces the weighted addition output $\mathbf{y} = \mathbf{Xw}$ by projecting $\mathbf{X}$ onto the subspace of weight vector $\mathbf{w}$ (set at the MRR weight bank). Following the same line of thought, we may rephrase the ICA formulation by treating $\mathbf{A^{-1}}$ as an equivalent column vector with each entry being an IC vector $\mathbf{e_i} (i = 1, \ldots, n)$ that projects $\mathbf{X}$ to a particular IC basis $\bar{s_i}(t) = \mathbf{Xe_i} (i = 1, \ldots, n)$. In that case, we frame our photonic ICA approach as a variate of projection pursuit [6], where we keep updating $\mathbf{w}$ until the projected representation is an optimal estimation of an IC (i.e., when $\mathbf{w}$ converges to a particular $\mathbf{e_i}$). This approach particularly does not require estimation on any model parameters as compared to the moment fitting algorithm recently proposed in [13].

We first apply photonic PCA [26] as a pre-processing step, where the applied weight vectors $\mathbf{w_1}, \ldots, \mathbf{w_n}$ converge to the PC vectors by projecting $\mathbf{y}$ to the subspace where the projection variance is maximized. The main purpose of performing photonic PCA first is to obtain the whitening matrix $\mathbf{V}$ to simplify the following photonic ICA. Conventional software-based ICA algorithms would directly apply $\mathbf{V}$ to whiten $\mathbf{X}$, and then supply the whitened mixtures $\mathbf{VX}$ as

Optics EXPRESS

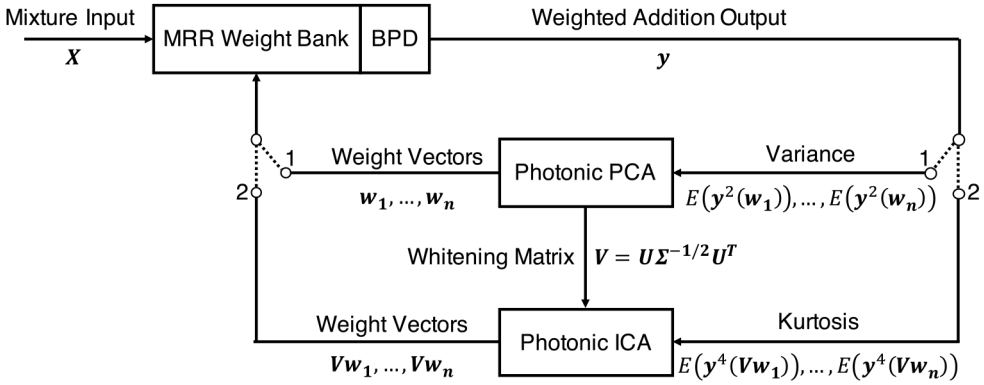

Fig. 2. Flowchart of the complete photonic ICA procedure exploiting the interaction between the photonic hardware (MRR weight bank plus BPD) and software (photonic PCA/ICA algorithms). First, the photonic hardware produces the weighted addition output $\mathbf{y}$ of the input mixtures $\mathbf{X}$. Next, the photonic PCA algorithm updates the weight vectors $\mathbf{w_1}, \ldots, \mathbf{w_n}$ (set at the MRR weight bank) to be the target PC vectors by maximizing the variance of $\mathbf{y}$ (when switch is on 1). Finally, the photonic ICA algorithm takes the whitening matrix $\mathbf{V}$ computed from photonic PCA results, and updates the weight vectors in the whitened subspace $\mathbf{Vw_1}, \ldots, \mathbf{Vw_n}$ to be the target IC vectors by maximizing the kurtosis of $\mathbf{y}$ (when switch is on 2). Both photonic PCA and ICA algorithms require multiple iterations for convergence. Detailed code implementations of photonic PCA can be found in [26], while code implementations of photonic ICA can be found in Appendix A of this manuscript.

the input to the subsequent ICA procedure. Instead, we introduce $\mathbf{V}$ as an input argument to the photonic ICA algorithm, so as to directly process the input mixtures rather than having to sample, store, and replay $\mathbf{VX}$. This is consistent with our efforts of performing photonic ICA without redundant waveform information, not to mention $\mathbf{VX}$ expands the size of $\mathbf{V}$ by $T/2$ times here where T is the number of samples taken at super-Nyquist rate.

4.1. ICA algorithm

We describe ICA algorithm as Algorithm 1 in Appendix A, which proceeds by first initializing multiple weight vectors $\mathbf{w_1}, .., \mathbf{w_n}$. However, the actual weight vectors applied at the MRR weight bank now become $\mathbf{Vw_1}, .., \mathbf{Vw_n}$, which will equivalently transform our ICA procedure to the whitened subspace of the input mixtures. More importantly, these weight vectors are constrained to have unit norm because a) the weight vector magnitude is not supposed to affect the kurtosis measurement of the weighted addition output, and b) we are only differed from the actual ICs by an orthogonal transformation after whitening (i.e., only the weight vector direction matters). Therefore, weight normalization is imposed throughout the algorithm execution (where "normalized" is used).

Our ICA pursuit algorithm borrows inspirations from the well-known Nelder-Mead method [37], aiming to converge all the weight vectors to the target IC vector by updating the weight vector associated with the smallest weighted addition output kurtosis at each iteration. Please refer to Algorithm 1 for the detailed code implementations on four types of update operations available: reflection, expansion, contraction, and shrinkage, which contribute to the final convergence collectively. The algorithm proceeds until reaching the termination condition, which is controlled by a convergence tolerance gauging the proximity of weight vectors. The algorithm can extract ICs sequentially by enforcing the Gram-Schimit process (i.e., deflationary orthogonalization) given the fact that IC vectors are orthogonal against each another (see Line 40 of Algorithm 1).

Optics EXPRESS

4.2. Ill-conditioning

The difficulty of ICA problem largely depends on the mixing condition where so-called ill-conditioning can increase the chance of non-separable ICs. In this work, we consider the following two basic forms of ill-conditioning:

a) Low channel separability: the transmission paths for ICs are close $a_1/a_3 \approx a_2/a_4$ (e.g., when the sources/receivers are close to each other), so that the received mixtures $x_1 = a_1s_1 + a_2s_2$, $x_2 = a_3s_3 + a_4s_4$ are similar (could be differed approximately by a scaling factor). We quantify the channel separability using the condition number of the mixing matrix $\mathbf{A}$ [38]

$$\kappa(\mathbf{A}) = ||\mathbf{A}|| \cdot ||\mathbf{A}^{-1}|| \tag{3}$$

where $||\cdot||$ stands for the maximum absolute column sum. The channels are most separable when $\kappa(\mathbf{A})_{min} = 1$ (e.g., if $a_1/a_3 = a_4/a_2 = \infty$), and least separable when $\kappa(\mathbf{A})_{max} = \infty$ (e.g., if $a_1/a_3 = a_2/a_4$).

b) Near-far problem: the ratio of received power levels of ICs is high (e.g., when the desired signal is far away while an undesired interferer is nearby). Suppose s_1 is the signal of interest, and s_2 is the signal of interference. Then, we can fix the received power level of s_2 while varying the received power level of s_1 by considering the following simple but illustrative mixing matrix

$$\mathbf{A} = \begin{bmatrix} \epsilon & 1 \\ 0 & 1 \end{bmatrix} \tag{4}$$

where ϵ controls the intensity ratio between two ICs in mixture $x_1 = \epsilon s_1 + s_2$. If both ICs have equal power enter the mixer, then $20 \cdot log_{10}(\epsilon)$ quantifies their signal-to-interference ratio (SIR) within mixture x_1.

5. Experimental results

In this section, we present the empirical results obtained from the two-channel photonic ICA experiment, demonstrating the feasibility of the proposed algorithm and the robustness under ill-conditioning cases above.

5.1. Channel separability case

We first present the experimental results of two-channel photonic ICA under various channel separability conditions. Table 1 lists the effective mixing matrix ($\mathbf{A}$) configured by the mixer in the experimental setup, and their associated condition number (κ) ranging from 1 to 105. We do not consider κ further beyond since prior ICA work has identified that $\kappa > 10$ already corresponds to badly-conditioned mixing matrix [39]. We first run the photonic ICA algorithm to find the IC vectors in free-running mode, and then apply those obtained IC vectors to record the corresponding IC waveforms in synchronized mode for evaluation purpose. For the sake of comparison, we also implement software-based ICA solution using the most popular FastICA algorithm [28] (see Appendix B for implementation information) and report its results.

The waveforms of the received mixtures and corresponding ICs associated with 4 typical κ values are shown in Fig. 3. On the left column, the received mixtures on both channels (RX1 and RX2) exhibit more similarity as κ increases, meaning the two mixing channels become alike (note how the mixtures are almost the same at $\kappa = 21$). The channel separability conditions have a direct impact on the accuracy of recovered ICs shown on the right column, where the red curves represent the measured outcome of photonic ICA procedure. IC1 is expected to be the square wave, while IC2 is expected to be the sinusoidal wave. When κ is small (e.g., $\kappa = 1$ or 5), the photonic ICA procedure can faithfully retrieve correct ICs; however, when κ is large (e.g., $\kappa = 10$ or 21), the photonic ICA procedure faces more difficulty of finding accurate ICs. The ICs

Optics EXPRESS

Table 1. ICA Performance Under Channel Separability Conditions

Mixing Matrix (**A**)	Condition Number (κ)	SNR (dB)	1^{st} IC		2^{nd} IC	
			FastICA	PhotonicICA	FastICA	PhotonicICA
			RMSE ± SD (%)	RMSE ± SD (%)	RMSE ± SD (%)	RMSE ± SD (%)
$\begin{bmatrix} 1 & 0 \\ 0 & 1 \end{bmatrix}$	1	22.70	8.04 ± 0.06	8.72 ± 0.23	7.80 ± 0.08	7.97 ± 0.13
$\begin{bmatrix} 0.8 & 0.4 \\ 0.4 & 0.9 \end{bmatrix}$	3	21.03	14.38 ± 0.09	14.65 ± 1.46	15.93 ± 0.10	17.88 ± 1.17
$\begin{bmatrix} 0.8 & 0.5 \\ 0.6 & 0.9 \end{bmatrix}$	5	21.88	21.04 ± 0.11	22.63 ± 1.51	22.45 ± 0.24	24.02 ± 0.99
$\begin{bmatrix} 0.8 & 0.6 \\ 0.5 & 0.7 \end{bmatrix}$	7	21.22	26.46 ± 0.15	28.03 ± 2.32	28.52 ± 0.16	29.07 ± 2.11
$\begin{bmatrix} 0.7 & 0.5 \\ 0.7 & 0.8 \end{bmatrix}$	10	21.38	30.61 ± 0.17	34.57 ± 2.36	32.60 ± 0.39	35.89 ± 2.07
$\begin{bmatrix} 0.7 & 0.8 \\ 0.4 & 0.6 \end{bmatrix}$	21	22.19	36.43 ± 0.24	40.78 ± 3.27	38.13 ± 0.81	39.58 ± 3.16
$\begin{bmatrix} 0.8 & 0.7 \\ 0.5 & 0.4 \end{bmatrix}$	65	22.14	44.71 ± 0.39	47.38 ± 3.66	46.88 ± 1.29	50.76 ± 3.91
$\begin{bmatrix} 0.8 & 0.7 \\ 0.6 & 0.5 \end{bmatrix}$	105	22.12	54.60 ± 0.64	58.58 ± 4.14	58.07 ± 1.81	61.35 ± 4.05

recovered by FastICA are plotted as black curves in parallel to demonstrate such difficulty results from the worsening of channel separability rather than the algorithm itself.

Table 1 summarizes quantitative photonic ICA performance under various channel separability conditions. For each κ value, we run the algorithm 6 times (all with newly-initialized random weight vectors) to study the robustness of the proposed approach. We are interested in a) the average root-mean-squared error (RMSE) between measured and ground-truth ICs among all 6 runs to quantify accuracy, and b) the standard deviation (SD) of measured ICs among all 6 runs to quantify repeatability. All values are obtained when both the measured and ground-truth ICs are temporally aligned and normalized to unit power (the scale of ICs does not matter in ICA problem). We also report the results of FastICA algorithm in the table.

While the accuracy of both FastICA and photonic ICA degrades with the increase of κ, their performance difference is limited throughout the κ values considered here. For the best case of $\kappa = 1$, photonic ICA achieves almost the same performance as FastICA, both claiming about 8% RMSE. For the worst case of $\kappa = 105$, both their RMSEs are over 50% with photonic ICA having about 4% more error than FastICA. The low accuracy of ICs at large κ stems directly from the inherent difficulty of decomposing two almost the same linear combinations into two different components. This difficulty holds even if the demixer has the full access to the mixing matrix, and the lack of knowledge on the mixing matrix in ICA settings only makes it worse.

The repeatability of both FastICA and photonic ICA worsens with respect to the increase of κ as well. However, the SDs of FastICA are mostly small (less than 1% for IC1, less than 2% for IC2), due to the comparatively invariant input mixtures sampled under super-Nyquist rate. In contrast, the SDs of photonic ICA express less stability. From the best case of $\kappa = 1$ to the worst case of $\kappa = 105$, the SD increases by about 4% for both ICs. We do not attribute this uncertainty to our statistics-based photonic ICA approach itself as [13] has demonstrated the histogram of weighted addition output are identical regardless of whether it is sampled under super-Nyquist rate or sub-Nyquist rate. Instead, the errors originate from our prototype photonic subsystem, particularly the instability of MRR weight bank that oversees the drifting of weights over time (we will have more discussions later about the reasons behind this phenomenon).

Optics EXPRESS

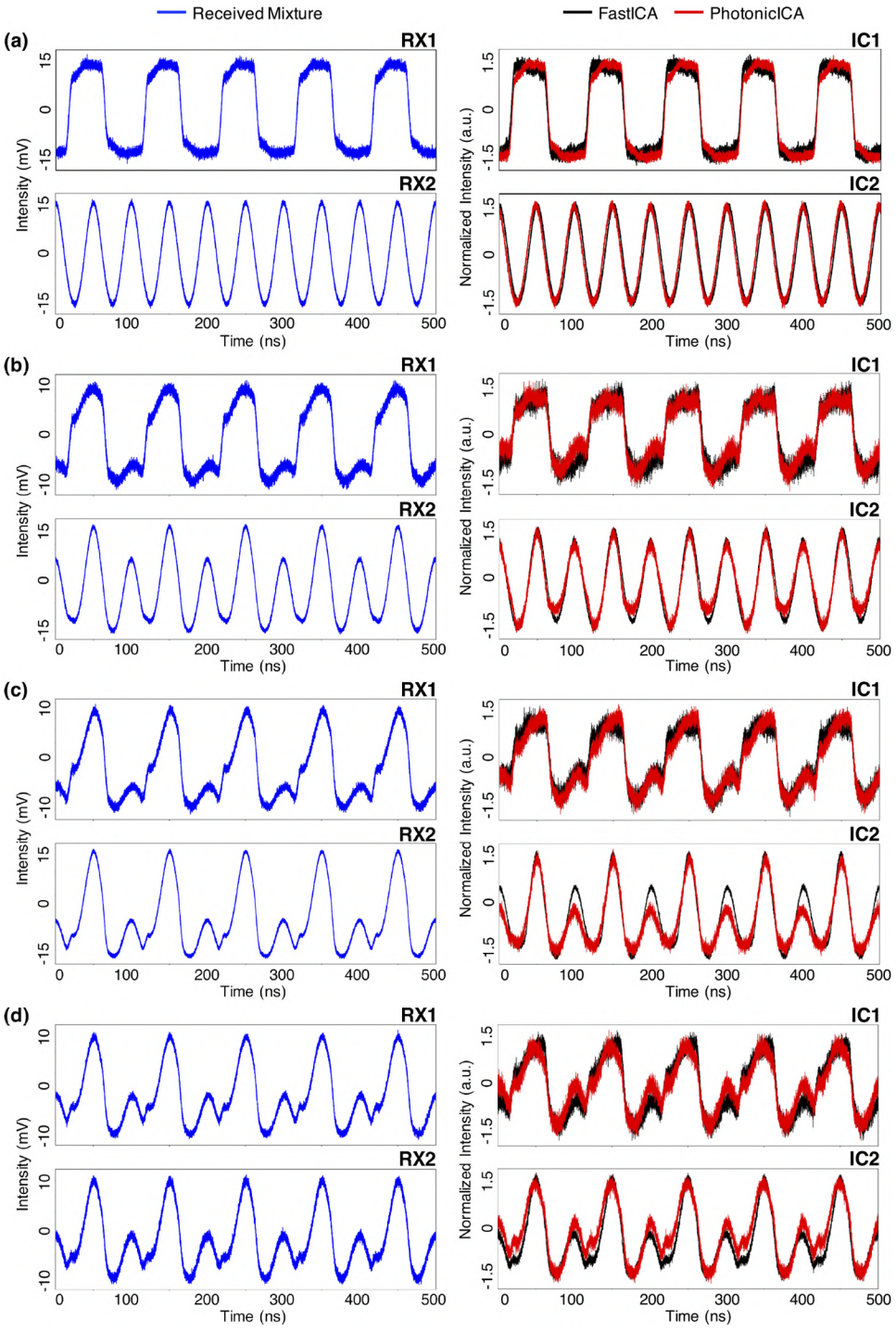

Fig. 3. Experimental waveforms of the received mixtures (left column) and corresponding ICs (right column) associated with 4 typical condition numbers of the mixing matrix: (a) $\kappa = 1$, (b) $\kappa = 5$, (c) $\kappa = 10$, (d) $\kappa = 21$. The degradation of channel separability conditions (from top to bottom) makes it more difficult for FastICA (black curves) and PhotonicICA (red curves) to retrieve correct ICs.

Optics EXPRESS

5.2. Near-far case

We next present the experimental results of two-channel photonic ICA under various near-far conditions. Table 2 lists the effective mixing matrix (**A**) configured by the mixer in the experimental setup, with ϵ ranging from +1.5 to -0.25. Here, we pick the square wave as signal of interest s_1 (i.e., far source), and the sinusoidal wave as signal of interference s_2 (i.e., near source). By setting them to have the same output power from AWGs, the SIR of these two sources in mixture $r_1 = \epsilon s_1 + s_2$ is in the range of 0 dB to −12.04 dB. The special case of SIR = 3.52 dB (top row) results from having the output power of AWG1 3.52 dB higher than that of AWG2 while keeping $\epsilon = 1$. We follow the same procedure of previous channel separability case by first running the photonic ICA algorithm to find the IC vectors in free-running mode, and then applying those obtained IC vectors to record the corresponding IC waveforms in synchronized mode for evaluation.

Table 2. ICA Performance Under Near-far Conditions

Mixing Matrix (**A**)	SIR (dB)	SNR (dB)	1^{st} IC (far source)		2^{nd} IC (near source)	
			FastICA	PhotonicICA	FastICA	PhotonicICA
			RMSE ± SD (%)	RMSE ± SD (%)	RMSE ± SD (%)	RMSE ± SD (%)
$\begin{bmatrix} 1.5 & 1 \\ 0 & 1 \end{bmatrix}$	3.52	23.26	8.91 ± 0.05	9.27 ± 0.67	9.34 ± 0.09	10.14 ± 0.48
$\begin{bmatrix} 1.0 & 1 \\ 0 & 1 \end{bmatrix}$	0	22.23	13.24 ± 0.14	14.72 ± 0.96	10.13 ± 0.10	11.03 ± 1.25
$\begin{bmatrix} 0.8 & 1 \\ 0 & 1 \end{bmatrix}$	−1.94	22.12	19.49 ± 0.10	21.57 ± 1.78	11.93 ± 0.13	12.13 ± 1.56
$\begin{bmatrix} 0.6 & 1 \\ 0 & 1 \end{bmatrix}$	−4.44	20.60	25.27 ± 0.13	28.46 ± 2.54	11.98 ± 0.19	12.65 ± 1.72
$\begin{bmatrix} 0.5 & 1 \\ 0 & 1 \end{bmatrix}$	−6.02	21.32	32.65 ± 0.16	35.41 ± 2.83	11.91 ± 0.15	13.59 ± 1.56
$\begin{bmatrix} 0.4 & 1 \\ 0 & 1 \end{bmatrix}$	−7.96	21.56	38.80 ± 0.31	41.95 ± 3.41	11.77 ± 0.14	13.67 ± 1.97
$\begin{bmatrix} 0.3 & 1 \\ 0 & 1 \end{bmatrix}$	−10.46	21.32	45.71 ± 0.56	49.01 ± 3.06	10.83 ± 0.13	12.29 ± 1.09
$\begin{bmatrix} 0.25 & 1 \\ 0 & 1 \end{bmatrix}$	−12.04	21.10	50.14 ± 0.83	54.93 ± 4.27	10.77 ± 0.15	11.19 ± 1.31

The waveforms of the received mixtures and corresponding ICs associated with 4 typical SIR values are shown in Fig. 4. On the left column, the received mixture on channel RX1 is a combination of both sources, while the received mixture on channel RX2 is the pure sinusoidal wave (given **A** used here). RX1 exhibits more similarity with the sinusoidal wave as SIR increases, since the power contribution of the square wave gradually diminishes from RX1. The impact of near-far conditions on recovered ICs is shown on the right column, where we are especially concerned with the recovery of square wave (IC1). When SIR is high (e.g., SIR = 0 dB or −4.44 dB), the photonic ICA procedure may faithfully retrieve correct IC1; however, when SIR is low (e.g., SIR = −7.96 dB or −12.04 dB), the photonic ICA procedure faces more difficulty of finding accurate IC1. The FastICA faces the same difficulty as in the black curves. The recovery of sinusoidal wave (IC2) is largely successful regardless of SIR values, because the final projection onto IC directions always involves a copy of its ground-truth on RX2.

Table 2 summarizes quantitative photonic ICA performance under various near-far conditions. Likewise, we run the algorithm 6 times for the same SIR value to obtain the average RMSE between measured and ground-truth ICs among all 6 runs, as well as the SD of measured ICs among all 6 runs. All values are obtained when both the measured and ground-truth ICs are

Optics EXPRESS

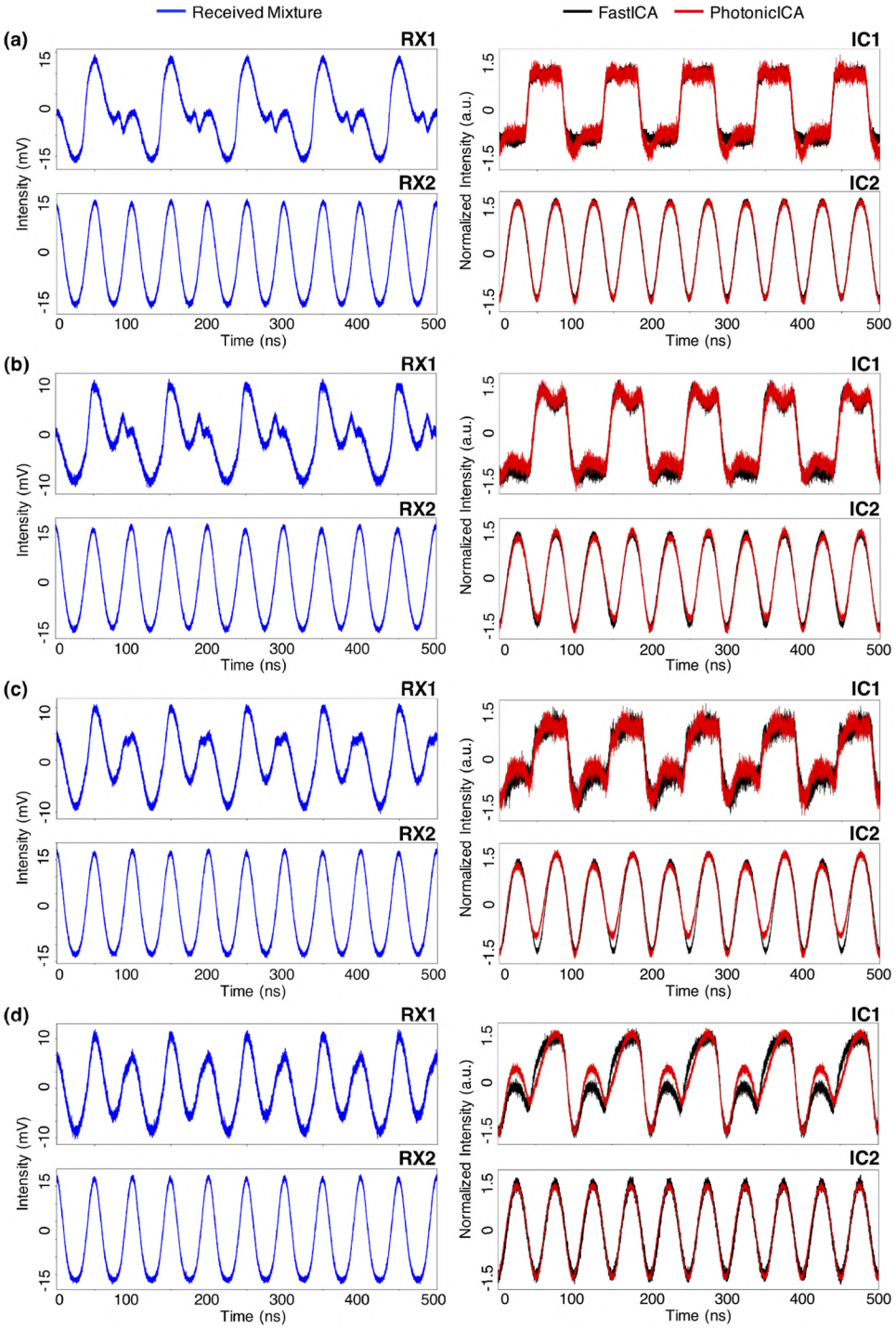

Fig. 4. Experimental waveforms of the received mixtures (left column) and corresponding ICs (right column) associated with 4 typical power ratios of the received power levels of ICs: (a) SIR = 0 dB, (b) SIR = −4.44 dB, (c) SIR = −7.96 dB, (d) SIR = −12.04 dB. Here, the square wave is the signal of interest (i.e., far source), while the sinusoidal wave is the signal of interference (i.e., near source). The decrease of the SIR (from top to bottom) makes it more difficult for FastICA (black curves, IC1) and PhotonicICA (red curves, IC1) to retrieve square waves. The recovery of sinusoidal wave (IC2) is largely successful thanks to the pure copy of it on the second mixture channel (RX2).

Optics EXPRESS

temporally aligned and normalized to unit power. We also report the results of FastICA algorithm in the table. Thanks to the additional copy of sinusoidal wave on RX2, we first notice that IC2 maintains stable performance across SIR values considered. The RMSEs of IC2 are less than 12% and 14% for FastICA and photonic ICA, respectively. The SDs of FastICA are limited to be less than 0.2%, while the SDs of photonic ICA are controlled below 2%.

As for the IC1 performance, the first row with positive SIR considers an exceptional case with more power of IC1 than that of IC2 in the received mixtures. Hence, the square wave (signal of interest) tends to be recognized with less difficulty, as evidenced by less than 10% RMSEs and less than 1% SDs measured for IC1 of both schemes. The second row with SIR = 0 dB can be treated as the base case where the received power levels are equal for both ICs. Under such circumstance, the photonic ICA approach realizes an RMSE that is only about 1% higher than that of FastICA. The rows below the base case with negative SIRs all put IC1 at a disadvantageous position of having less power than that of IC2 in the received mixtures. This certainly challenges the demixing mechanism to extract the lower power IC1 buried beneath the high power IC2, and both methods result in over 50% RMSEs when SIR = −12.04 dB. While FastICA faces the same accuracy deterioration along with the decrease of SIR, its SD performance (generally less than 1%) is better than that of photonic ICA (raised to over 4% when SIR = −12.04 dB), due to the weight drifting problem mentioned before.

6. Numerical results

The above experimental demonstration of two-channel photonic ICA illustrates the effectiveness of the proposed approach for proof-of-concept purpose. In this section, we demonstrate numerical results that identify the fundamental operating regime of the photonic ICA approach under more comprehensive mixing conditions (e.g., the effect of noise, higher κ or lower ϵ) that are difficult to control/achieve in real experiment.

One issue we have not discussed but plays a critical role in ICA is the effect of noise, especially the Gaussian noise that can greatly reduce the non-Gaussianity of ICs. From the mathematical perspective, the noise effect fits the simple ICA model by adding an extra noise term to the noise-free mixtures: $\mathbf{X} = \mathbf{AS} + \mathbf{N}$, where $\mathbf{N}$ contains noise components for individual mixing channel. In our numerical simulation, we emulate the channel noise using the Gaussian distribution with zero mean and varying variance, since the Gaussian noise dominates in most transmission media [40]. Here, we define the signal-to-noise ratio (SNR) as the power ratio between the two terms of the received mixtures, and present the photonic ICA performance taking into consideration a wide range of SNR values in Fig. 5. We simulate with the same sources as our experimental demonstration, i.e., one square wave and one sinusoidal wave. It is worth mentioning that we also run FastICA in parallel and its results turn out to overlap with those of our photonic ICA algorithm (so we don't show separate figures), which once again validates the fidelity of the proposed approach.

Figure 5(a) shows how channel noise affects the RMSE versus κ ranging from 1 to 1000 (our experiment only reaches about 100), where we make the following observations: a) The amount of noise defines the lower bound of RMSE the demixer is able to deliver (when $\kappa = 1$), e.g., RMSE is about 3% for SNR = 30 dB. This is because the Gaussian noise corrupts the non-Gaussianity of ICs by bringing the IC kurtosis closer to Gaussian (and thus making it difficult for ICA algorithm to converge on its maximum). It also explains why ICs could still hold about 8% RMSE in our experiment (top row in Table 1), even if the channel separability condition is optimal. b) The channel noise dominates the ICA performance when SNR is low. As can be seen from those low SNR curves, the RMSE only has small changes when $\kappa < 10$ and saturate beyond $\kappa > 10$. For the extreme case of SNR = 0 dB, the RMSE behaves as if it is not affected by κ value at all by fluctuating around 80% throughout the κ range considered. c) The channel separability condition dominates the ICA performance when SNR is high. Those high SNR

Optics EXPRESS

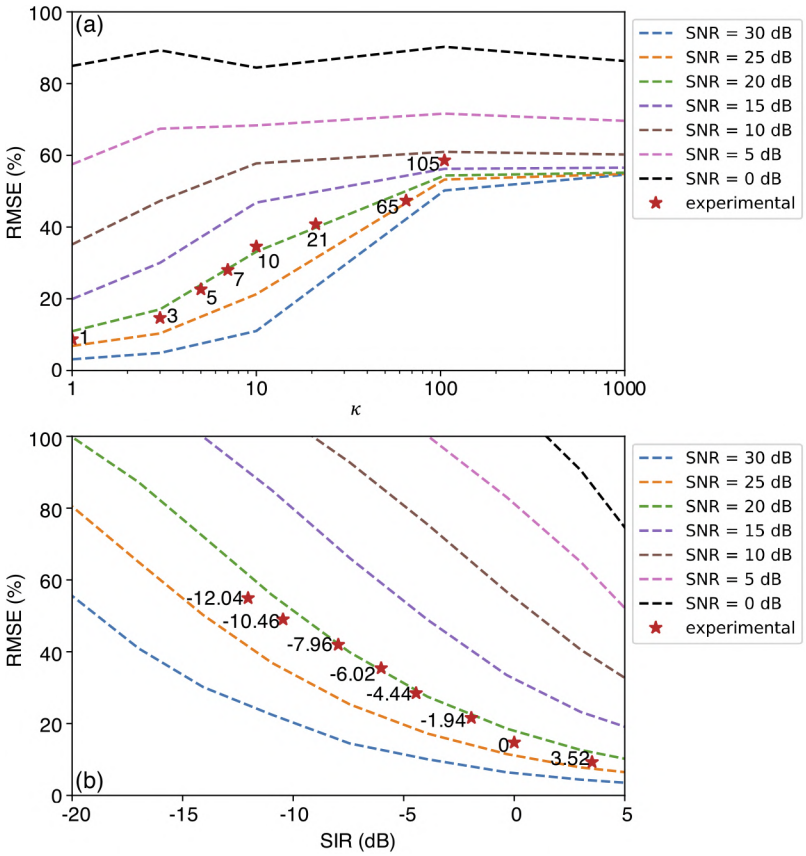

Fig. 5. Numerical investigations of the photonic ICA performance considering the channel noise added in the mixing process. Curves associated with 7 typical SNR values between 0 dB and 30 dB are displayed to show the noise effect on: (a) RMSE versus κ ranging from 1 to 1000. The red asterisks represent our experimental data of channel separability conditions whose SNR range is between 21 dB and 23 dB. The label next to each asterisk stands for the corresponding κ value. (b) RMSE versus SIR ranging from -20 dB to 5 dB. The red asterisks represent our experimental data of near-far conditions whose SNR range is between 20 dB and 24 dB. The label next to each asterisk stands for the corresponding SIR value.

curves witness a clear RMSE degradation with the increase of κ, e.g., RMSE increases from 3% to 50% for SNR = 30 dB. We also plot our discrete experimental points (RMSE of IC1) of channel separability case whose SNR values (third column in Table 1) are between 21 dB and 23 dB, and notice most of these points locate between SNR curves of 20 dB and 25 dB.

Figure 5(b) shows how channel noise affects the RMSE versus SIR ranging from -20 dB to 5 dB (our experiment only reaches about -12 dB). The major takeaway is that the channel noise itself can act as an additional source of interference. For low SNR curves, the channel noise acts as the dominating signal of interference, and leads to ultra-high RMSE even if SIR value is positive. For high SNR curves, the channel noise may still serve as a contributing factor of interference if its power is comparable to that of the actual signal. For example, the green curve of SNR = 20 dB has 100% RMSE at SIR = −20 dB. This is because the signal of interest shares equal power level as the channel noise at this point, which makes it difficult for the demixing mechanism to distinguish one from another. We also plot our discrete experimental points (RMSE of IC1) of near-far case whose SNR values (third column in Table 2) are between 20 dB and 24 dB, which illustrates a good fitting between SNR curves of 20 dB and 25 dB.

Optics EXPRESS

Overall, our numerical simulation identifies the operating regime of our photonic ICA approach, which provides useful guidance on estimating what degree of IC accuracy to expect given different channel noise levels, channel separabilities and near-far conditions.

7. Discussion

We have demonstrated the first photonic ICA experiment using an on-chip MRR weight bank. There is room for improvements in both accuracy and repeatability. The performance gap between photonic ICA and FastICA is due to: a) the additional system noise generated by the photonic subsystem, including the optical noise generated at DFBs, MZMs, and the electrical noise produced by the BPD; and b) the signal degradation caused by insertion loss to the chip, which can be improved by integrating laser sources, modulator, and detectors together with the MRR weight bank [41,42]. However, this would face a suite of technical challenges especially the ones aiming for hybrid platforms interconnecting both III-V materials and silicon [43,44].

In terms of repeatability deficiency of photonic ICA, the weight drifting at MRR weight bank is the major challenge that needs to be addressed. While we have demonstrated, to the best of our knowledge, the highest weight accuracy/precision achieved on MRR weight banks, maintaining the weights at an acceptable level over a reasonable period of time can still be challenging when it comes to control an analog weighting element. The main reasons behind weight drifting are two-fold: a) cross-talk between neighboring MRRs where the channel power from one MRR may leak into another as MRRs are only close to be critically-coupled with the bus waveguide in practice; and b) thermal fluctuations that cannot be completely prevented by the temperature controller as we keep sourcing current to the on-chip heating elements to reconfigure the MRR weight bank. The former issue is likely to find its solution from optimizing the MRR design with higher Q factor/finesse. The latter issue can be addressed by better weight locking mechanisms such as the one through phase change material [45], or switching to other non-thermal tuning approaches such as the one through carrier-depletion effect [46].

In this work, we restrict ourselves to two-channel mixing-demixing process not because our method cannot be extended to higher dimensions, but because the two-channel photonic ICA is the base case for higher dimensional photonic ICA scheme. The successful demonstration of a two-channel photonic ICA suffice proof-of-principle purpose, and makes the extension to higher dimensions straightforward (numerically speaking, [26] has demonstrated that similar pursuit algorithm can scale up to at least 8 channels). Another reason behind our focus on two-channel photonic ICA originates from the implementation cost that the number of required discrete DFBs, MZMs, SMs all scale linearly with the number of channels present. We can overcome such limitation via ongoing efforts that aim to integrate every components aforementioned onto the same chip.

We also acknowledge it is not practical to generalize our scheme to arbitrary dimensions due to the following scaling limitations. The first limitation stems from photonic weight bank itself since both the resonator finesse F and free spectral range FSR limits the number of channels N. For example, for platforms containing MRRs whose Q-factors is 10-20k and finesse is 133, N is estimated to be upper bounded at 32 for 1-pole MRR weight bank and 110 for 2-pole MRR weight bank [19,47,48]. These limitations are imposed mainly because our implementation is based on WDM, while other forms of multiplexing (e.g., polarization-division multiplexing) can potentially relieve these restrictions. Another limitation stems from the proposed photonic ICA algorithm that learns ICs in the decremental order of kurtosis. In general, there exists an error increment from lower-order IC to higher-order IC; for example, the error difference between IC1 and IC2 is around 0-3% in our two-channel photonic ICA experiment under various channel separability conditions. We observe the possibility of mitigating this problem by reducing the tolerance parameter used in the ICA algorithm. However, there is a trade-off between the convergence time and the error accumulations among ICs, and trade-offs like this should be taken into account when applying the proposed approach for real-time ICA applications.

Optics EXPRESS

Algorithm 1: ICA algorithm

Input: weighted addition output $\mathbf{y}$; whitening matrix $\mathbf{V}$;
Parameters: convergence tolerance ϵ, reflection coefficient β, expansion coefficient γ, contraction coefficient ρ, shrinkage coefficient σ;
Output: IC vectors $\mathbf{e_1}$ and $\mathbf{e_2}$;

initialize n normalized random weight vectors $\mathbf{w_i}(i = 1, ..., n)$;
for $i = 1 : n$ **do**
  compute the normalized whitened weight vectors $\mathbf{v_i} = \mathbf{V}\mathbf{w_i}$;
  apply $\mathbf{v_i}$ to the weight bank and obtain the resulted $\mathbf{y}(\mathbf{v_i})$;
  compute the objective function, i.e., the kurtosis of $\mathbf{y}$: $f(\mathbf{w_i}) = kurt(\mathbf{y}^4(\mathbf{v_i}))$;
end for
among $f(\mathbf{w_i})(i = 1, ..., n)$, find $f_{max} = max(f(\mathbf{w_i}))$, $f_{min} = min(f(\mathbf{w_i}))$;
set $\mathbf{w_{max}} = argmax(f(\mathbf{w_i}))$, $\mathbf{w_{min}} = argmin(f(\mathbf{w_i}))$;
if $|f_{max} - f_{min}| \leq \epsilon$ **then**
  return $\mathbf{e_1} = \mathbf{w_{max}}$, $\mathbf{e_2} = \mathbf{e_1^T}$;
end if
while $|f_{max} - f_{min}| > \epsilon$ **do**
  compute the centroid of all weight vectors: $\mathbf{w_{cen}} = E(\mathbf{w_i})$;
  compute the normalized reflected weight vector: $\mathbf{w_{ref}} = \mathbf{w_{cen}} + \beta(\mathbf{w_{cen}} - \mathbf{w_{min}})$;
  compute the normalized whitened reflected weight vector: $\mathbf{v_{ref}} = \mathbf{V}\mathbf{w_{ref}}$;
  if $f_{min} < f(\mathbf{w_{ref}}) = kurt(\mathbf{y}^4(\mathbf{v_{ref}})) < f_{max}$ **then**
    $\mathbf{w_{min}} = \mathbf{w_{ref}}$ and update f_{min}, $\mathbf{w_{min}}$;
  else if $f(\mathbf{w_{ref}}) \geq f_{max}$ **then**
    compute the normalized expanded weight vector: $\mathbf{w_{exp}} = \mathbf{w_{cen}} + \gamma(\mathbf{w_{ref}} - \mathbf{w_{cen}})$;
    compute the normalized whitened expanded weight vector: $\mathbf{v_{exp}} = \mathbf{V}\mathbf{w_{exp}}$;
    if $f(\mathbf{w_{ref}}) < f(\mathbf{w_{exp}}) = kurt(\mathbf{y}^4(\mathbf{v_{exp}}))$ **then**
      $\mathbf{w_{max}} = \mathbf{w_{exp}}$ and update $f_{max} = f(\mathbf{w_{exp}})$;
    else
      $\mathbf{w_{max}} = \mathbf{w_{ref}}$ and update $f_{max} = f(\mathbf{w_{ref}})$;
    end if
  else if $f(\mathbf{w_{ref}}) \leq f_{min}$ **then**
    compute the normalized contracted weight vector: $\mathbf{w_{con}} = \mathbf{w_{cen}} + \rho(\mathbf{w_{min}} - \mathbf{w_{cen}})$;
    compute the normalized whitened contracted weight vector: $\mathbf{v_{con}} = \mathbf{V}\mathbf{w_{con}}$;
    if $f(\mathbf{w_{con}}) = kurt(\mathbf{y}^4(\mathbf{v_{con}})) > f(\mathbf{w_{min}})$ **then**
      $\mathbf{w_{min}} = \mathbf{w_{con}}$ and update f_{min}, $\mathbf{w_{min}}$;
    else
      for $i = 1 : n$ **do**
        replace with normalized weight vector $\mathbf{w_i} = \mathbf{w_{max}} + \sigma(\mathbf{w_i} - \mathbf{w_{max}})$;
        compute the normalized whitened weight vector $\mathbf{v_i} = \mathbf{V}\mathbf{w_i}$;
      end for
      update f_{max}, f_{min}, and $\mathbf{w_{max}}$, $\mathbf{w_{min}}$;
    end if
  end if
end while
return $\mathbf{e_1} = \mathbf{w_{max}}$, $\mathbf{e_2} = \mathbf{e_1^T}$.

Optics EXPRESS

8. Conclusion

In this paper, we used an on-chip MRR weight bank to project the multi-dimensional signals onto a single-dimensional representation i.e., the weighted addition operation. Our prototype implementation produced mixtures under controllable conditions, and set a new record of 5.7 bits of accuracy and 6.9 bits of precision for controlling the MRR weight bank. More importantly, we performed photonic ICA assuming that we are ignorant of the real-time waveform information of the input mixtures and weighted addition output. We overcome this observability constraint via a novel ICA algorithm that works with the pure observation of the kurtosis measurement of the weighted addition output. We carried out two-channel photonic ICA experiment to study its performance under various channel separability and near-far conditions, which is close to the results of software-based FastICA method. The numerical simulation further corroborated the feasibility of our scheme, and identified the operating regime of photonic ICA given different noise effects.

This work can be significantly extended to include high-dimensional experimental demonstration, larger-scale integration, and convergence acceleration. In terms of enabling advanced BSS techniques in particular, we would need to test our approach in conjunction with multi-antenna systems transmitting RF signals over the air. The goal would be to outperform current approaches that rely on digitizing ultra-redundant multi-dimensional signals, and lack the tunability across multi-frequency bands (desired by most wide-band RF systems) [49].

Appendix A: ICA algorithm

See Algorithm 1.

Appendix B: FastICA implementation

We use the sklearn.decomposition.fastICA method of Python scikit-learn package to implement FastICA. For fair comparison, we assign the customized fourth-order moment as the 'fun' argument such that the algorithm will use kurtosis in its optimization.

Funding

Defense Advanced Research Projects Agency (HR-00111990049); National Science Foundation (ECCS-1642962).

Acknowledgments

Fabrication support was provided via the Natural Sciences and Engineering Research Council of Canada (NSERC) Silicon Electronic-Photonic Integrated Circuits (SiEPIC) Program and the Canadian Microelectronics Corporation (CMC). Devices were fabricated at Advanced Micro Foundry (AMF) A*STAR foundry in Singapore.

Disclosures

The authors declare no conflicts of interest.

References

1. C. Jutten and J. Herault, "Blind separation of sources, part i: An adaptive algorithm based on neuromimetic architecture," Signal Process. **24**(1), 1–10 (1991).
2. P. Comon, "Independent component analysis a new concept?" Signal Process. **36**(3), 287–314 (1994).
3. P. O. Hoyer and A. Hyvärinen, "Independent component analysis applied to feature extraction from colour and stereo images," Network-Comp. Neural. **11**(3), 191–210 (2000).
4. M. S. Bartlett, J. R. Movellan, and T. J. Sejnowski, "Face recognition by independent component analysis," IEEE Trans. Neural Netw. **13**(6), 1450–1464 (2002).

Optics EXPRESS

5. Q. V. Le, W. Y. Zou, S. Y. Yeung, and A. Y. Ng, "Learning hierarchical invariant spatio-temporal features for action recognition with independent subspace analysis," in "*CVPR 2011*," (2011), pp. 3361–3368.
6. A. Hyvärinen and E. Oja, "Independent component analysis: algorithms and applications," Neural Netw. **13**(4-5), 411–430 (2000).
7. M.-Z. Poh, D. J. McDuff, and R. W. Picard, "Non-contact, automated cardiac pulse measurements using video imaging and blind source separation," Opt. Express **18**(10), 10762–10774 (2010).
8. G. Salimi-Khorshidi, G. Douaud, C. F. Beckmann, M. F. Glasser, L. Griffanti, and S. M. Smith, "Automatic denoising of functional mri data: combining independent component analysis and hierarchical fusion of classifiers," NeuroImage **90**, 449–468 (2014).
9. T. Kim, H. T. Attias, S.-Y. Lee, and T.-W. Lee, "Blind source separation exploiting higher-order frequency dependencies," IEEE Trans. Audio Speech Lang. Process. **15**(1), 70–79 (2007).
10. E. Vincent, R. Gribonval, and C. Févotte, "Performance measurement in blind audio source separation," IEEE Trans. Audio Speech Lang. Process. **14**(4), 1462–1469 (2006).
11. I. F. Akyildiz, W.-Y. Lee, M. C. Vuran, and S. Mohanty, "Next generation/dynamic spectrum access/cognitive radio wireless networks: A survey," Computer Netw. **50**(13), 2127–2159 (2006).
12. M. P. Chang, E. C. Blow, M. Z. Lu, J. J. Sun, and P. R. Prucnal, "Rf characterization of an integrated microwave photonic circuit for self-interference cancellation," IEEE Trans. Microwave Theory Tech. **66**(1), 596–605 (2018).
13. A. N. Tait, T. F. de Lima, P. Y. Ma, M. P. Chang, M. A. Nahmias, B. J. Shastri, P. Mittal, and P. R. Prucnal, "Blind source separation in the physical layer," in *"52nd Annual Conference on Information Sciences and Systems (CISS)"*, (IEEE, 2018), pp. 1–6.
14. R. H. Walden, "Analog-to-digital converter survey and analysis," IEEE J. Select. Areas Commun. **17**(4), 539–550 (1999).
15. T. Sundstrom, B. Murmann, and C. Svensson, "Power dissipation bounds for high-speed nyquist analog-to-digital converters," IEEE Trans. Circuits Syst. I **56**(3), 509–518 (2009).
16. P. Jebashini, R. Uma, P. Dhavachelvan, and H. K. Wye, "A survey and comparative analysis of multiply-accumulate (mac) block for digital signal processing application on asic and fpga," J. Appl. Sci. **15**(7), 934–946 (2015).
17. R. K. Mongia, J. Hong, P. Bhartia, and I. J. Bahl, *RF and microwave coupled-line circuits* (Artech house, 2007).
18. A. N. Tait, M. A. Nahmias, B. J. Shastri, and P. R. Prucnal, "Broadcast and weight: an integrated network for scalable photonic spike processing," J. Lightwave Technol. **32**(21), 4029–4041 (2014).
19. A. N. Tait, A. X. Wu, T. F. de Lima, E. Zhou, B. J. Shastri, M. A. Nahmias, and P. R. Prucnal, "Microring weight banks," IEEE J. Sel. Top. Quantum Electron. **22**(6), 312–325 (2016).
20. J. Komma, C. Schwarz, G. Hofmann, D. Heinert, and R. Nawrodt, "Thermo-optic coefficient of silicon at 1550 nm and cryogenic temperatures," Appl. Phys. Lett. **101**(4), 041905 (2012).
21. Q. Xu and R. Soref, "Reconfigurable optical directed-logic circuits using microresonator-based optical switches," Opt. Express **19**(6), 5244–5259 (2011).
22. J. Wang, H. Shen, L. Fan, R. Wu, B. Niu, L. T. Varghese, Y. Xuan, D. E. Leaird, X. Wang, F. Gan, A. M. Weiner, and M. Qi, "Reconfigurable radio-frequency arbitrary waveforms synthesized in a silicon photonic chip," Nat. Commun. **6**(1), 5957 (2015).
23. K. Vandoorne, P. Mechet, T. Van Vaerenbergh, M. Fiers, G. Morthier, D. Verstraeten, B. Schrauwen, J. Dambre, and P. Bienstman, "Experimental demonstration of reservoir computing on a silicon photonics chip," Nat. Commun. **5**(1), 3541 (2014).
24. P. R. Prucnal and B. J. Shastri, *Neuromorphic Photonics* (CRC Press, 2017).
25. A. N. Tait, T. F. Lima, E. Zhou, A. X. Wu, M. A. Nahmias, B. J. Shastri, and P. R. Prucnal, "Neuromorphic photonic networks using silicon photonic weight banks," Sci. Rep. **7**(1), 7430 (2017).
26. P. Y. Ma, A. N. Tait, T. F. de Lima, S. Abbaslou, B. J. Shastri, and P. R. Prucnal, "Photonic principal component analysis using an on-chip microring weight bank," Opt. Express **27**(13), 18329–18342 (2019).
27. A. N. Tait, P. Y. Ma, T. F. De Lima, E. C. Blow, M. P. Chang, M. A. Nahmias, B. J. Shastri, and P. R. Prucnal, "Demonstration of multivariate photonics: blind dimensionality reduction with integrated photonics," J. Lightwave Technol. **37**(24), 5996–6006 (2019).
28. A. Hyvarinen, "Fast and robust fixed-point algorithms for independent component analysis," IEEE Trans. Neural Netw. **10**(3), 626–634 (1999).
29. A. Hyvärinen, J. Karhunen, and E. Oja, *Independent component analysis* (John Wiley & Sons, 2004).
30. A. Hyvärinen, "New approximations of differential entropy for independent component analysis and projection pursuit," in "*Advances in neural information processing systems*," (1998), pp. 273–279.
31. D. T. Pham and P. Garat, "Blind separation of mixture of independent sources through a quasi-maximum likelihood approach," IEEE Trans. Signal Process. **45**(7), 1712–1725 (1997).
32. A. Tait, T. F. de Lima, P. Y. Ma, A. Jha, H.-T. Peng, H. Miller, and P. R. Prucnal, "lightwave-lab/lightlab: Version 1.0.5," (2018). DOI: 10.5281/zenodo.1436917.
33. A. N. Tait, H. Jayatilleka, T. F. D. Lima, P. Y. Ma, M. A. Nahmias, B. J. Shastri, S. Shekhar, L. Chrostowski, and P. R. Prucnal, "Feedback control for microring weight banks," Opt. Express **26**(20), 26422–26443 (2018).
34. A. E.-J. Lim, J. Song, Q. Fang, C. Li, X. Tu, N. Duan, K. K. Chen, R. P.-C. Tern, and T.-Y. Liow, "Review of silicon photonics foundry efforts," IEEE J. Sel. Top. Quantum Electron. **20**(4), 405–416 (2014).

Optics EXPRESS

35. H. Jayatilleka, K. Murray, M. Á. Guillén-Torres, M. Caverley, R. Hu, N. A. Jaeger, L. Chrostowski, and S. Shekhar, "Wavelength tuning and stabilization of microring-based filters using silicon in-resonator photoconductive heaters," Opt. Express **23**(19), 25084–25097 (2015).
36. T. Baehr-Jones, R. Ding, A. Ayazi, T. Pinguet, M. Streshinsky, N. Harris, J. Li, L. He, M. Gould, Y. Zhang, A. E.-J. Lim, T.-Y. Liow, S. H.-G. Teo, G.-Q. Lo, and M. Hochberg, "A 25 gb/s silicon photonics platform," arXiv preprint arXiv:1203.0767 (2012).
37. J. A. Nelder and R. Mead, "A simplex method for function minimization," Comput. J. **7**(4), 308–313 (1965).
38. D. A. Belsley, E. Kuh, and R. E. Welsch, *Regression diagnostics: Identifying influential data and sources of collinearity* (John Wiley & Sons, 2005).
39. A.. Hyvarinen, "Fast ica for noisy data using gaussian moments," in "*ISCAS'99. Proceedings of the 1999 IEEE International Symposium on Circuits and Systems VLSI (Cat. No. 99CH36349)*," (IEEE, 1999), pp. 57–61.
40. A. Goldsmith, *Wireless communications* (Cambridge University, 2005).
41. J. S. Orcutt, B. Moss, C. Sun, J. Leu, M. Georgas, J. Shainline, E. Zgraggen, H. Li, J. Sun, M. Weaver, S. Urošević, M. Popović, R. J. Ram, and V. Stojanović, "Open foundry platform for high-performance electronic-photonic integration," Opt. Express **20**(11), 12222–12232 (2012).
42. Y. Arakawa, T. Nakamura, Y. Urino, and T. Fujita, "Silicon photonics for next generation system integration platform," IEEE Commun. Mag. **51**(3), 72–77 (2013).
43. G. Roelkens, L. Liu, D. Liang, R. Jones, A. Fang, B. Koch, and J. Bowers, "Iii-v/silicon photonics for on-chip and intra-chip optical interconnects," Laser Photonics Rev. **4**(6), 751–779 (2010).
44. M. J. Heck, J. F. Bauters, M. L. Davenport, J. K. Doylend, S. Jain, G. Kurczveil, S. Srinivasan, Y. Tang, and J. E. Bowers, "Hybrid silicon photonic integrated circuit technology," IEEE J. Sel. Top. Quantum Electron. **19**(4), 6100117 (2013).
45. C. Ríos, Y. Zhang, S. Deckoff-Jones, H. Li, J. B. Chou, H. Wang, M. Shalaginov, C. Roberts, C. Gonçalves, V. Liberman, T. Gu, J. Kong, K. Richardson, and J. Hu, "Reversible switching of optical phase change materials using graphene microheaters," in "*Conference on Lasers and Electro-Optics*," (Optical Society of America, 2019), p. SF2H.4.
46. P. Dong, S. Liao, D. Feng, H. Liang, D. Zheng, R. Shafiiha, C.-C. Kung, W. Qian, G. Li, X. Zheng, A. V. Krishnamoorthy, and M. Asghari, "Low vpp, ultralow-energy, compact, high-speed silicon electro-optic modulator," Opt. Express **17**(25), 22484–22490 (2009).
47. A. N. Tait, T. Ferreira de Lima, M. P. Chang, M. A. Nahmias, B. J. Shastri, and P. R. Prucnal, "Application regime and distortion metric for multivariate rf photonics," in "*IEEE Optical Interconnects Conference (OI)*," (2017), p. 25–26.
48. A. N. Tait, A. X. Wu, T. F. de Lima, M. A. Nahmias, B. J. Shastri, and P. R. Prucnal, "Two-pole microring weight banks," Opt. Lett. **43**(10), 2276–2279 (2018).
49. P. Russer Tuan-Do-Hong, "Signal processing for wideband smart antenna array applications," IEEE Microw. Mag. **5**(1), 57–67 (2004).